

Klaus Werner · Thorsten Nagel · Thomas Rauch

Non-LTE modeling of supernova-fallback disks

Received: date / Accepted: date

Abstract We present a first detailed spectrum synthesis calculation of a supernova-fallback disk composed of iron. We assume a geometrically thin disk with a radial structure described by the classical α -disk model. The disk is represented by concentric rings radiating as plane-parallel slabs. The vertical structure and emission spectrum of each ring is computed in a fully self-consistent manner by solving the structure equations simultaneously with the radiation transfer equations under non-LTE conditions. We describe the properties of a specific disk model and discuss various effects on the emergent UV/optical spectrum.

We find that strong iron-line blanketing causes broad absorption features over the whole spectral range. Limb darkening changes the spectral distribution up to a factor of four depending on the inclination angle. Consequently, such differences also occur between a blackbody spectrum and our model. The overall spectral shape is independent of the exact chemical composition as long as iron is the dominant species. A pure iron composition cannot be distinguished from silicon-burning ash. Non-LTE effects are small and restricted to few spectral features.

Keywords Radiative transfer; scattering · Neutron stars · Infall, accretion, and accretion disks

PACS 95.30.Jx · 97.60.Jd · 98.35.Mp

1 Introduction

Anomalous X-ray pulsars (AXPs) are slowly rotating ($P_{\text{rot}} = 5 - 12$ s) young ($\leq 100\,000$ yr) isolated neutron stars. Their X-ray luminosities ($\approx 10^{36}$ erg/s) greatly exceed the rates of rotational energy loss ($\approx 10^{33}$ erg/s). It is now generally believed that AXPs are magnetars with

magnetic field strengths greater than 10^{14} G and that their X-ray luminosity is powered by magnetic energy (Woods & Thompson 2006). As an alternative explanation the X-ray emission was attributed to accretion from a disk that is made up of supernova-fallback material (van Paradijs et al. 1995, Chatterjee et al. 2000, Alpar 2001). The fallback-disk model has difficulties to explain IR/optical emission properties of AXPs. When compared with disk models, the faint IR/optical flux suggests that any disk around AXPs must be very compact (e.g. Perna et al. 2000, Israel et al. 2004).

The discovery of optical pulsations in 4U 0142+61 which have the same period like the X-ray pulsations (Kern & Martin 2002) appears to be a strong argument against the disk model. It was argued that reprocessing of the pulsed NS X-ray emission in the disk cannot explain the high optical pulsed fraction, because disk radiation would be dominated by viscous dissipation and not by reprocessed NS irradiation (Kern & Martin 2002). Ertan & Cheng (2004), on the other hand, showed that these optical pulsations can be explained either by the magnetar outer gap model or by the disk-star dynamo model. Therefore, the observation of optical pulsations is not an argument against the disk model. A spectral break in the optical spectrum of 4U 0142+61 was discovered by Hulleman et al. (2004). This was also taken as an argument against the disk model because the authors do not expect such strong features from a thermally emitting disk. The recent discovery of mid-IR emission from this AXP (Wang et al. 2006), however, has strongly rekindled the interest in studies of fallback-disk emission properties. While this mid-IR emission was attributed to a cool, passive (X-ray irradiated) dust debris disk by Wang et al. (2006), it was shown by Ertan on this conference that it can be explained with a model for an active, dissipating gas disk. If true, then the disk emission properties allow to conclude on important quantities, e.g., the magnetic field strength of the neutron star can be derived from the inner disk radius.

Independent hints for the possible existence of fallback disks come from pulsars with particular spin-down

K. Werner, T. Nagel, T. Rauch
Institut für Astronomie und Astrophysik
Universität Tübingen, Germany
E-mail: werner@astro.uni-tuebingen.de

Table 1 Characteristics of the nine rings that compose the disk model. Surface mass density Σ and emergent flux (expressed as T_{eff}) follow from the α disk prescription. The Rosseland optical depth τ_{Ross} at the disk midplane, the mass density ρ and gravity $\log g$ at optical depth unity follow from our computations of the detailed vertical ring structure. The last column denotes the fraction of the disk area that is made up by each ring model in order to compute disk-integrated spectra.

Ring	R [1000 km]	Σ [g/cm ²]	T_{eff} [1000 K]	$\log \tau_{\text{Ross}}^{\text{midplane}}$	$\log \rho(\tau_{\text{Ross}} = 1)$ [g/cm ³]	$\log g(\tau_{\text{Ross}} = 1)$ [cm/s ²]	% area fraction
1	2.0	2.9	305	3.1	-6.1	7.7	0.0025
2	2.5	2.8	258	3.2	-6.2	7.5	0.01
3	3.5	2.7	201	3.3	-6.4	7.2	0.034
4	6.0	2.6	135	3.5	-6.0	6.7	0.084
5	9.0	2.6	100	3.7	-5.9	6.4	0.19
6	14	2.5	72	3.3	-6.4	6.0	0.62
7	25	2.3	46	3.5	-6.9	5.5	1.70
8	40	2.2	33	3.9	-7.1	5.1	33
9	200	1.9	9.8	3.8	-7.6	3.6	64

properties. For example, the discrepancy between the characteristic age and the supernova age of the pulsar B1757-24 was explained by the combined action of magnetic dipole radiation and accretion torques (Marsden et al. 2001). Even more, the presence of jets from pulsars such like the Crab and Vela can possibly be explained by disk-wind outflow interacting with and collimating the pulsar wind (Blackman & Perna 2004).

A fallback-disk model was proposed in order to explain the X-ray enhancement following a giant flare of the Soft Gamma Repeater SGR 1900+14 (Ertan & Alpar 2003). The X-ray light curve is interpreted in terms of the relaxation of a fallback disk that has been pushed back by the gamma-ray flare. This model can also explain the long-term X-ray and IR enhancement light curves of the AXP 1E 2259+58 following a major bursting epoch (Ertan et al. 2006).

The presence of a fallback disk around the stellar remnant of SN 1987A has been invoked in order to explain its observed lightcurve which deviates from the theoretical one for pure radioactive decay (Meyer-Hofmeister 1992). From the non-detection of any UV/optical point source in the supernova remnant, however, tight constraints for the disk extension can be derived (Graves et al. 2005).

To our best knowledge, the emission from fallback disks in all studies was hitherto modeled with blackbody spectra. In view of the importance of disk models for the quantitative interpretation of observational data it is highly desirable to construct more realistic models by detailed radiation-transfer calculations.

2 Radial disk structure

For the modeling we employ our computer code AcDc (Nagel et al. 2004), that calculates disk spectra under the following assumptions. The radial disk structure is calculated assuming a stationary, Keplerian, geometrically thin α -disk (Shakura & Sunyaev 1973). As pointed out by Menou et al. (2001), for a comparison with ob-

servational data one probably has to use a more elaborate model, because near the outer disk edge the viscous dissipation and hence the surface mass density decline stronger with increasing radius than in an α -disk. However, the purpose of the present paper is to look for differential effects of various assumptions. Qualitatively, these effects can be expected to be independent of the detailed radial disk structure. In any case, it would be no problem to carry out the computations presented here with different radial structures.

The α -disk model is fixed by four global input parameters: Stellar mass M_* and radius R_* of the accretor, mass accretion rate \dot{M} , and the viscosity parameter α . For numerical treatment the disk is divided into a number of concentric rings. For each ring with radius R our code calculates the detailed vertical structure, assuming a plane-parallel radiating slab.

In contrast to a (planar) stellar atmosphere, which is characterized by T_{eff} and $\log g$, a particular disk ring with radius R is characterized by the following two parameters, which follow from the global disk parameters introduced above. The first parameter measures the dissipated and then radiated energy. It can be expressed in terms of an effective temperature T_{eff} :

$$T_{\text{eff}}^4(R) = [1 - (R_*/R)^{1/2}] 3GM_*\dot{M}/8\sigma\pi R^3.$$

The second parameter is the half surface mass density Σ of the disk ring:

$$\Sigma(R) = [1 - (R_*/R)^{1/2}] \dot{M}/3\pi\bar{w}.$$

σ and G are the Stefan-Boltzmann and gravitational constants, respectively. \bar{w} is the depth mean of viscosity $w(z)$, where z is the height above the disk mid-plane. The viscosity is given by the standard α -parametrization as a function of the total (i.e. gas plus radiation) pressure, but numerous other modified versions are used in the literature. We use a formulation involving the Reynolds number Re , as proposed by Kriz & Hubeny (1986). We chose $Re = 15000$ which corresponds to $\alpha \approx 0.01$.

For the results presented here we selected the following input parameter values. The neutron star mass

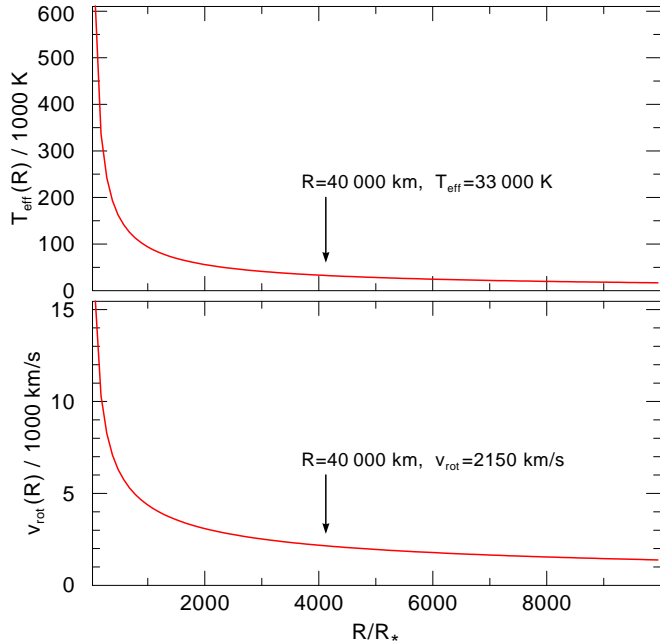


Fig. 1 Radial disk structure: Effective temperature (top panel) and Keplerian rotation velocity (bottom panel). Arrows mark a reference point at a distance of $R=40\,000$ km (about 4000 stellar radii R_*) from the neutron star as discussed in the text.

is $1.4 M_\odot$. The radii of the inner and outer disk edges are 2000 and 200 000 km, respectively. The disk is represented by nine rings or, more precisely, by nine radial grid points. The radiation integrated over the whole disk is then computed by assigning a weight to each point's spectrum that resembles the area fraction that it represents. The main characteristics of the disk at the radial grid points are given in Tab. 1. The mass-accretion rate was set to $\dot{M} = 3 \cdot 10^{-9} M_\odot/\text{yr}$. Fig. 1 shows the radial run of T_{eff} . We also display the Keplerian rotation velocity for the later discussion of our results. The radial distance from the neutron star is expressed in units of the NS radius which is set to $R_* = 9.7$ km. But note from the above equations that the disk model is essentially independent of the stellar radius for large distances from the neutron star.

While $\Sigma(R)$ and $T_{\text{eff}}(R)$ in columns 3 and 4 of Tab. 1 follow from the α -disk assumption, the quantities in the next three columns are the result from our detailed vertical structure calculations described below. It shows that the entire disk model is optically thick. The Rosseland optical depth at the disk midplane $\tau_{\text{Ross}}^{\text{midplane}} > 1000$ at all radii. We also tabulate the mass density and the gravity at unity optical depth. That demonstrates that the conditions in the line forming regions of the disk resemble those in white dwarfs at the inner disk radii up to main sequence stars at the outer disk radii. The strength of Stark line broadening therefore strongly depends on the distance of the emitting region from the neutron star.

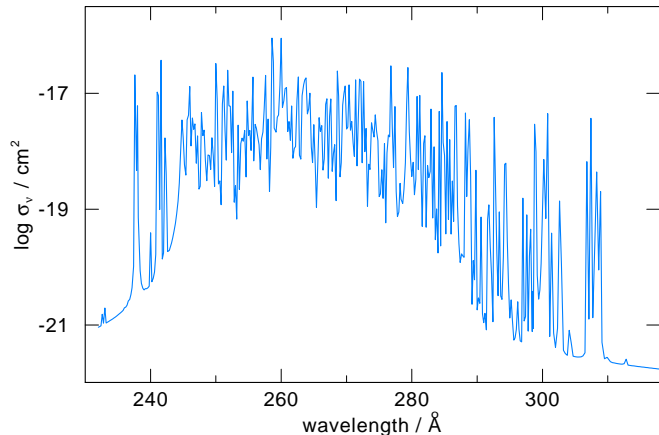


Fig. 2 Photon cross-section for a superline in the Fe IV ion (between superlevels number 1 and 7).

3 Vertical disk structure

The vertical structure of each disk ring is determined from the simultaneous solution of the radiation transfer equations plus the structure equations. The latter ones invoke radiative and hydrostatic equilibrium plus charge conservation. The structure equations also consist of the non-LTE rate equations for the atomic population densities. The solution of this set of highly non-linear integro-differential equations is performed using the Accelerated Lambda Iteration (ALI) technique (Werner & Husfeld 1985, Werner 1986, Werner et al. 2003).

The total observed disk spectrum, which depends on the inclination angle, is finally obtained by intensity integration over all rings accounting for rotational Doppler effects.

3.1 Radiation transfer, hydrostatic and radiative equilibrium

We consider the radiation transfer equation for the intensity I_ν at frequency ν :

$$\mu \frac{\partial I_\nu(\mu, z)}{\partial z} = -\kappa_\nu(z) I_\nu(\mu, z) + \eta_\nu(z)$$

with the opacity κ_ν and the emissivity η_ν . z measures the geometrical height above the disk midplane and μ is the cosine of the inclination angle i . The equation is solved using a short characteristics method. Opacities and emissivities are computed using atomic population densities that are obtained by solving the non-LTE rate equations. Our code allows for the irradiation of the disk by the central source, however, the results presented here are computed with zero incident intensity.

The radiation-transfer equations plus vertical structure equations are solved like in the stellar atmosphere case, but accounting for two basic differences. First, the gravity (entering the hydrostatic equation for the total,

Table 2 Summary of non-LTE model atoms for silicon, sulfur, and iron. The numbers in brackets at the iron ions give the number of individual lines summed up into superlines. Employed for a specific test run, the silicon and sulfur model atoms are tailored to the conditions encountered in disk ring number 8.

element	ion	NLTE levels	lines	
Si	III	6	4	
	IV	16	44	
	V	1	0	
S	III	1	0	
	IV	6	4	
	V	14	16	
	VI	1	0	
Fe	I	7	25	(141 821)
	II	7	25	(218 490)
	III	7	25	(301 981)
	IV	7	25	(1 027 793)
	V	7	25	(793 718)
	VI	8	33	(340 132)
	VII	7	22	(86 504)
	VIII	7	27	(8 724)
	IX	7	25	(36 843)
	X	7	28	(45 229)
	XI	1	0	

i.e. gas plus radiation, pressure) is not constant with depth, but increases with z . The gravity is the vertical component of the gravitational acceleration exerted by the central object (self-gravitation of the disk is negligible):

$$g = z GM_{\star}/R^3.$$

Second, the energy equation for radiative equilibrium balances the dissipated mechanical energy and the net radiative losses:

$$9/4 \rho w G\Sigma/R^3 = 4\pi \int_0^{\infty} (\eta_{\nu} - \kappa_{\nu} J_{\nu}) d\nu,$$

where ρ and J_{ν} denote mass density and mean intensity, respectively. In the case of a stellar atmosphere the left-hand side of this equation vanishes and we get the usual radiative equilibrium equation. The solution is obtained by a generalized Unsöld-Lucy scheme and yields the vertical temperature structure.

Having calculated the vertical structures and spectra of the individual disk rings, the ring spectra are integrated to get the spectrum of the whole accretion disk:

$$I_{\nu}(i) = \cos(i) \int_{R_i}^{R_o} \int_0^{2\pi} I_{\nu}(i, \phi, r) r d\phi dr.$$

Here, R_i and R_o denote the inner and outer radius of the disk, and ϕ is the azimuthal angle. At this stage, the Keplerian rotation velocity v_{rot} is taken into account by assigning a Doppler shift of $\Delta\nu = \frac{v}{c} v_{\text{rot}} \sin \phi \sin i$ to the intensity emerging from a specific azimuthal ring sector.

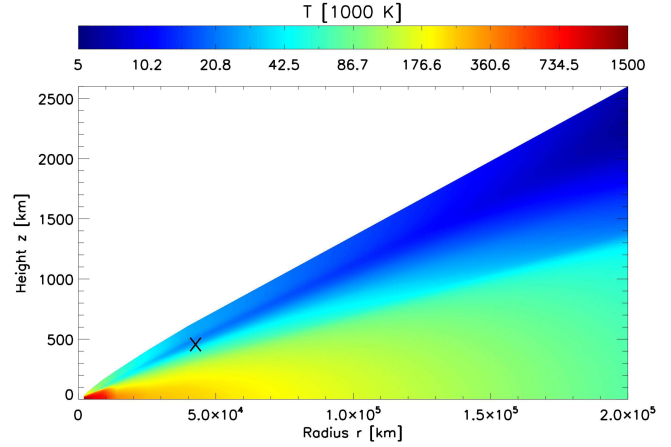


Fig. 3 This cut perpendicular to the midplane shows the temperature structure of the disk. Note that the vertical scale (height above the midplane) is expanded. The height-to-radius ratio is about 0.015. The cross marks the depth at $R=40\,000$ km where $\tau_{\text{Ross}} = 1$.

3.2 Non-LTE rate equations

For each atomic level i the rate equation describes the equilibrium of rates into and rates out of this level and, thus, determine the occupation numbers n_i :

$$n_i \sum_{i \neq j} P_{ij} - \sum_{j \neq i} n_j P_{ji} = 0.$$

The rate coefficients P_{ij} have radiative and electron collisional components: $P_{ij} = R_{ij} + C_{ij}$. The radiative downward rate for example is given by:

$$R_{ji} = \left(\frac{n_i}{n_j}\right)^* 4\pi \int_0^{\infty} \frac{\sigma_{ij}(\nu)}{h\nu} \left(\frac{2h\nu^3}{c^2} + J_{\nu}\right) e^{-h\nu/kT} d\nu.$$

$\sigma_{ij}(\nu)$ is the photon cross-section and $(n_i/n_j)^*$ is the Boltzmann LTE population ratio.

The blanketing by millions of lines from iron arising from transitions between some 10^5 levels can only be attacked with the help of statistical methods (Anderson 1989, Dreizler & Werner 1993). At the outset, model atoms are constructed by combining many thousands of levels into a relatively small number of superlevels. The respective line transitions are grouped into superlines connecting these superlevels. In this case, the population densities of the superlevels are computed from the rate equations, in which the photon cross-sections $\sigma_{ij}(\nu)$ in the radiative rates R_{ij} do not contain only a single line profile but all individual lines that are combined into a superline. As an example we show such a cross-section in Fig. 2. The complete spectrum of our disk model ($\lambda=4\text{--}300\,000$ Å) is sampled by 30 700 frequency points.

The model atoms that we have created for our disk calculations are summarized in Tab. 2. Most important is the iron model atom. It comprises the first eleven ionisation stages and a total number of more than 3 million

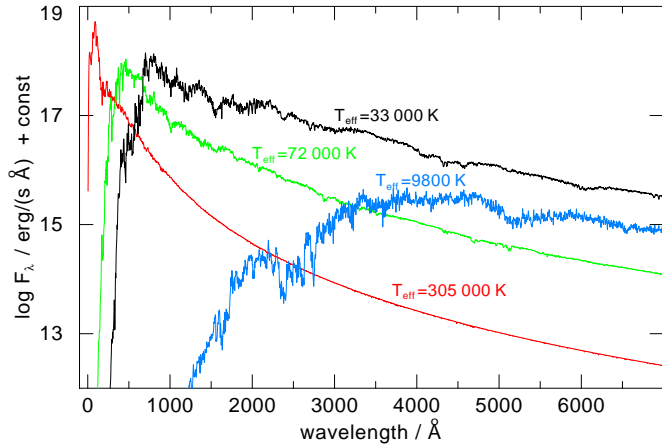


Fig. 4 Relative contribution of single disk rings to the total disk flux. For clarity, we only show the fluxes from rings number 1, 6, 8, and 9). The flux from ring 8 at $R=40\,000$ km with $T_{\text{eff}}=33\,000$ K dominates the total disk spectrum at UV/optical wavelengths.

lines. Atomic data are taken from Kurucz (1991) and the Opacity and Iron Projects (TIPTOPbase¹).

3.3 Disk composition

The chemical composition of the supernova fallback material in the disk is not exactly known. It depends on the amount of mass that goes into the disk. A disk with a small mass (say $\leq 0.001 M_{\odot}$) will be composed of silicon-burning ash (Menou et al. 2001). For simplicity, the results presented here are obtained by assuming a pure-iron composition. It turns out that the emergent spectrum is insensitive against the exact composition as long as iron is the dominant species (Sect. 4.1). For a respective test run for one specific ring we assumed a composition that represents a silicon-burning ash. It contains iron (80% mass fraction) as well as silicon and sulfur by 10% each.

3.4 Disk model properties

Fig. 3 displays the temperature structure of the disk. The temperature varies between 1.5 million K at the midplane at the inner disk edge down to 6000 K in the upper layers at the outer disk edge. At all radii the vertical run of the temperature decreases almost monotonously with height above the midplane. A mild temperature reversal in the uppermost disk layers occurs. This turns out to be a non-LTE effect, because the respective LTE model has a strictly monotonous temperature run. We will discuss the consequences of this effect in Sect. 4.2.

Which disk regions contribute to the total disk spectrum and to what extent? In Fig. 4 we plot the emergent

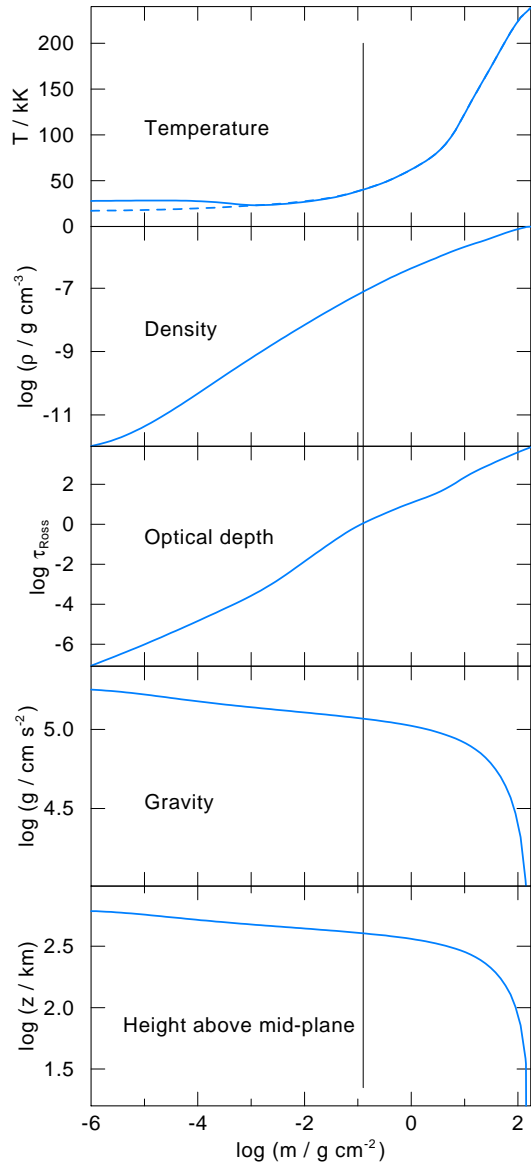


Fig. 5 Vertical stratification of the disk at $R=40\,000$ km (ring 8, $T_{\text{eff}}=33\,000$ K). The quantities are plotted against the column mass density that is measured from the disk surface to the midplane (from left to right). The vertical line at $\log m = -0.9$ denotes the depth where $\tau_{\text{Ross}} = 1$. The dashed curve in the top panel shows the temperature structure of a respective LTE model.

astrophysical flux from the area of four disk rings (rings 1, 6, 8, and 9, see Tab. 1), i.e., the computed flux per cm^2 is weighted with the ring area. The spectral flux distribution of the innermost ring with $T_{\text{eff}}=305\,000$ K has its peak value in the soft X-ray region. The contribution of this innermost region to the optical/UV spectrum is negligible. Cutting of the disk at this inner radius ($R=2000$ km), therefore, is justified if this spectral range is of interest. The disk region that is dominating the UV/optical flux is represented by ring 8 with $T_{\text{eff}}=33\,000$ K. Its radius is $40\,000$ km, that is about

¹ <http://vizier.u-strasbg.fr/topbase/>

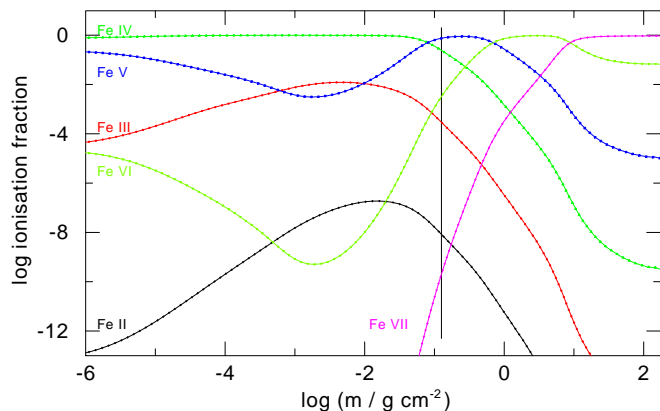


Fig. 6 Vertical iron ionisation structure at $R=40\,000$ km (ring 8, $T_{\text{eff}}=33\,000$ K). The vertical line at $\log m = -0.9$ denotes the depth where $\tau_{\text{Ross}} = 1$. The dominant iron opacities in the line forming regions are from Fe III-VI.

4000 neutron star radii. Its spectrum is dominated by strong blends of the numerous iron lines. Further out in the disk the effective temperature decreases and the flux contribution to the UV/optical spectrum decreases, too. Our outermost ring (number 9) has $T_{\text{eff}}=9800$ K, its flux maximum is at $\lambda=4000$ Å and it is fainter than the inner neighbor ring 8 over the whole spectral range. Cutting off the disk at this outer radius ($R=200\,000$ km) therefore does not affect the UV/optical spectral region.

4 Results

Because ring 8 is a representative disk region that determines the UV/optical spectrum, we will discuss its properties in more detail in the following three subsections, addressing the effects of chemical composition, non-LTE physics, and limb darkening on the spectrum. The radius of this ring is marked by arrows in Fig. 1 and by a cross in Fig. 3.

In Fig. 5 we show the vertical structure of the disk at this radius ($R=40\,000$ km). We plot the run of several quantities on a column-mass scale, measured inward from the surface toward the midplane of the disk. The vertical line at $\log m = -0.9$ marks the depth at which $\tau_{\text{Ross}} = 1$, i.e., the region of spectral line formation. The temperature shows a strong increase towards the midplane and, as already mentioned, a mild temperature reversal in the optically thin surface layers. Together with the temperature run, the panels showing the mass density and gravity structure indicate that their values in the line forming region are comparable to those encountered in hot subdwarfs. The lowest panel shows that the disk height H at this distance from the NS is ≈ 600 km, i.e. $R/H = 0.015$.

In Fig. 6 we show the vertical ionisation structure of iron in the disk at $R=40\,000$ km. The dominant ionisation stages in the line forming regions are Fe III-VI.

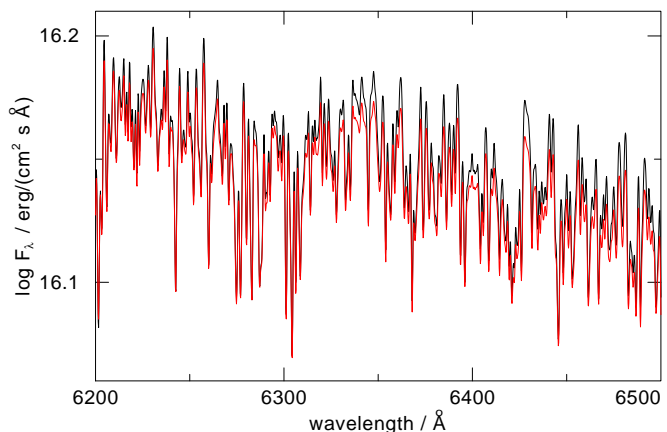


Fig. 7 Detail from the emergent disk spectrum at $R=40\,000$ km (ring 8, $T_{\text{eff}}=33\,000$ K). We compare a pure iron composition (black line) with a silicon-burning ash composition (red line). The differences are marginal.

At the midplane Fe VII is dominant. The temperature at any depth is so high that Fe I-II do not significantly contribute to the spectrum.

4.1 Effects of chemical composition

In Fig. 7 we show the flux spectrum of ring 8 in the wavelength range $\lambda=6200$ – 6500 Å. It has been calculated for a pure iron composition as well as for a Fe/Si/S=80/10/10 composition representing silicon-burning ash. The difference between the spectra is very small, because they are completely dominated by the extremely large number of iron lines. We conclude that the exact disk composition is not affecting the spectrum as long as iron is the dominant species.

While silicon and sulfur do not affect the overall spectrum by continuous background opacities, line features can be seen in the computed spectra, e.g. the Si IV resonance line in the UV. The line depth reaches about 50% of the continuum level but it would be difficult to detect even in medium resolution spectra when the disk inclination is high and the spectra are Doppler broadened by rotation.

4.2 Significance of non-LTE effects

For our particular disk model we expect that non-LTE effects are not very large. This is because of the relatively high gravities in the line forming regions, ranging between $\log g=3.6$ in the outermost ring with $T_{\text{eff}}=9800$ K and $\log g=7.7$ in the innermost region with $305\,000$ K. In Fig. 8 we compare the spectra of an LTE and a non-LTE model of disk ring 8 in the wavelength range $\lambda=1800$ – 2900 Å, where the largest deviations were found. Indeed, non-LTE physics affects only narrow spectral regions. Only there, flux differences occur to an extent that the

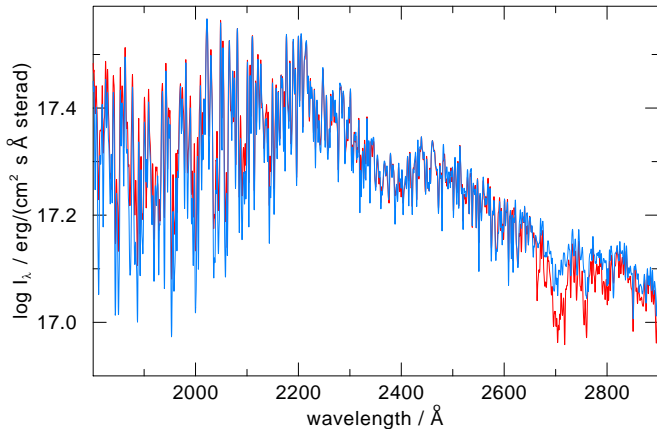


Fig. 8 Comparison of LTE and NLTE emergent disk intensities (red and blue lines, respectively) at $R=40\,000$ km (ring 8, $i = 87^\circ$, $T_{\text{eff}}=33\,000$ K).

equivalent width of line blends changes by a factor of two. Accordingly, the temperature structures of both models deviate only in the uppermost layers of the disk (see top panel of Fig. 5) and, hence, only strong spectral lines that are still optically thick can be affected.

4.3 Limb darkening effects

Our model spectra show distinct limb-darkening effects. The situation is similar to the stellar atmosphere case (center-to-limb variation of the specific intensity). Looking face-on we see into deeper and hotter (and thus “brighter”) layers of the disk when compared to a more edge-on view. In Fig. 9 we compare the specific intensity emitted by ring 8 (per unit area) for a high and a low inclination angle. Overall, the “edge-on” spectrum is roughly a factor of two fainter than the “face-on” spectrum in the optical region. The difference increases towards the UV and amounts to a factor of about three. We conclude that limb darkening effects are important when disk dimensions are to be estimated from magnitude measurements.

It is also interesting to compare the intensities with a blackbody spectrum (Fig. 9). Depending on the wavelength band, the blackbody over- or underestimates the “real” spectrum up to a factor of two in the optical and a factor of four in the UV.

4.4 Rotational broadening

We have seen that the spectrum of an iron-dominated disk is characterized by strong blends of a large number of lines. At some wavelengths broad spectral features appear. It remains to be seen if Doppler effects from disk rotation smears out these features or if they could still be detectable. From the bottom panel of Fig. 1 we see that rotational broadening amounts to $\approx \sin i \cdot 2000$ km/s

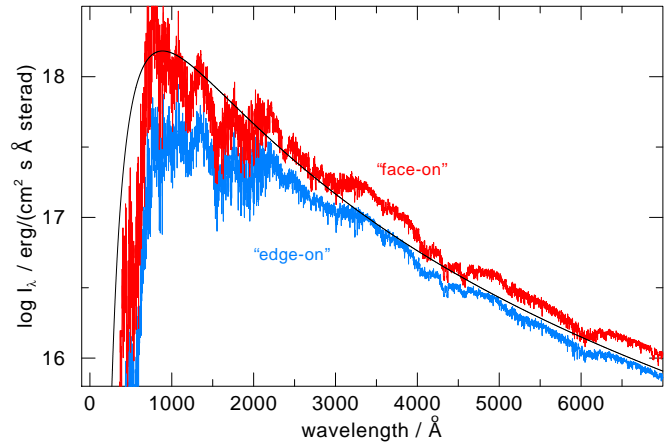


Fig. 9 Effect of limb darkening: Specific intensity of the disk at $R=40\,000$ km (ring 8) seen under two inclination angles, namely 87° (i.e. almost edge-on, blue) and 18° (i.e. almost face-on, red). For comparison we also show a blackbody spectrum with $T=T_{\text{eff}}=33\,000$ K.

at $R=40\,000$ km, corresponding to an orbital period of about two minutes. When seen almost edge-on, this rotational velocity is equivalent to a Doppler broadening of about $\Delta\lambda=25$ Å at $\lambda 4000$ Å which clearly smears out any individual line profiles. In Fig. 10 we display the rotationally broadened spectrum of the entire disk model, seen under three different inclination angles. It is obvious that the broad line blends are so prominent that they do not disappear even for an almost edge-on view of the disk.

Among the strongest features is a 200 Å wide line blend at $\lambda 1500$ Å with an absorption depth of about 50% relative to the continuum. Should the disk be cooler, then disk regions with $T_{\text{eff}}\approx 9000$ K could dominate the optical emission and the disk spectrum might look more like that emitted by ring 9 in our model (Fig. 4). Strong iron-line blanketing could cause a spectral break. This contrasts with a statement in Hulleman et al. (2004), where the spectral break observed in the optical energy distribution of the AXP 4U 0142+61 is suggested as an argument against disk emission.

5 Summary and outlook

We have computed a model for a supernova-fallback disk in order to study its structure and optical/UV emission properties. We assumed an α -disk for the radial structure and performed detailed non-LTE radiation transfer calculations for the vertical structure and spectrum synthesis. The input parameters were:

Neutron star mass: $1.4 M_\odot$
 Inner and outer disk edge radii: $R=2000$ and $200\,000$ km
 Mass-accretion rate: $\dot{M} = 3 \cdot 10^{-9} M_\odot/\text{yr}$.

We have identified that the disk region in the vicinity

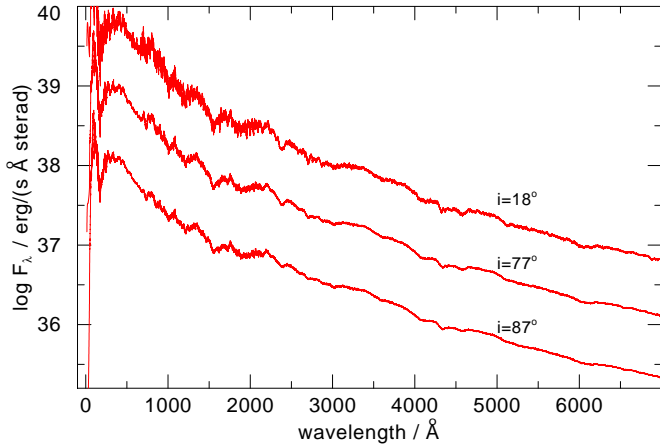


Fig. 10 Complete disk spectrum including Kepler rotation broadening, seen under three inclination angles. The broad iron-line blends are detectable even in the almost edge-on case.

of $R=40\,000$ km is the main contributor to the total disk spectrum at UV/optical wavelengths. We therefore investigated in some detail the disk properties at this radius.

We summarize our results as follows:

- The overall disk spectrum is independent of the detailed chemical composition as long as iron is the dominant species. In particular, a pure-iron composition is spectroscopically indistinguishable from a silicon-burning ash composition.
- The overall disk spectrum is hardly influenced by non-LTE effects, however, equivalent widths of individual line blends can change by a factor of two.
- Limb darkening affects the overall disk spectrum (in addition to the geometric foreshortening factor $\cos i$). Depending on inclination and spectral band, the disk intensity varies up to a factor of three.
- Depending on the inclination, the disk flux can be a factor of two higher or lower compared to a blackbody radiating disk.
- Strong iron line blanketing causes broad (> 100 Å) spectral features that could be detectable even from almost edge-on disks. Disks that are cooler than our model (because of a lower mass-accretion rate) could even exhibit a spectral break in the optical band due to massive line blanketing.

We stress that these results hold strictly only for our particular disk model. In order to arrive at more general results a systematic parameter study (disk extent, accretion rate) of the disk emission is necessary. Also, it needs to be investigated in detail how fine the subdivision of the disk in a number of rings is necessary in order to achieve a computed spectrum with a certain accuracy. In addition, deviations from the α -disk model must be studied. Another important point will be the inclusion of disk irradiation by the X-ray emission from the neutron

star. This will reveal the relative importance of viscous dissipation and reprocessed irradiation that is discussed in the context of simultaneous optical and X-ray pulsations in the AXP 4U 0142+61. At the moment we do not dare to make any prediction how this affects the results presented here.

The innermost disk ring has a very high effective temperature and its flux distribution peaks in the soft X-ray band. It needs to be investigated systematically under which conditions (inclination, inner disk radius, accretion rate) the innermost disk regions can contribute to the thermal spectrum of the magnetars.

Acknowledgements T.R. was supported by the German Ministry of Economy and Technology through the German Aerospace Center (DLR) under grant 50 OR 0201.

References

1. Alpar, M. A. *ApJ*, **554**, 1245 (2001)
2. Anderson, L. S. *ApJ*, **339**, 558 (1989)
3. Blackman, E. G., & Perna, R. *ApJ*, **601**, L71 (2004)
4. Chatterjee, P., Hernquist, L., & Narayan, R. *ApJ*, **534**, 373 (2000)
5. Dreizler, S., & Werner, K. *A&A*, **278**, 199 (1993)
6. Ertan, Ü., this conference
7. Ertan, Ü., & Alpar, M. A. *ApJ*, **593**, L93 (2003)
8. Ertan, Ü., & Cheng, K. S. *ApJ*, **605**, 840 (2004)
9. Ertan, Ü., Göğüş, E., & Alpar, M. A. *ApJ*, **640**, 435 (2006)
10. Graves, G. J. M., Challis, P. M., Chevalier, R. A., et al. *ApJ*, **629**, 944 (2005)
11. Hulleman, F., van Kerkwijk, M. H., & Kulkarni, S. R. *A&A*, **416**, 1037 (2004)
12. Israel, G. L., Rea, N., Mangano, V., et al. *ApJ*, **603**, L97 (2004)
13. Kern, B., & Martin, C. *Nature*, **417**, 527 (2002)
14. Kriz, S., & Hubeny, I. *Bull. Astron. Inst. Czechoslovakia*, **37**, 129 (1986)
15. Kurucz, R. L. in: Crivellari, L., Hubeny, I., Hummer, D. G. (ed.) *Stellar Atmospheres: Beyond Classical Models*, NATO ASI Series C, **341**, 441 (1991)
16. Marsden, D., Lingenfelter, R. E., & Rothschild, R. E. *ApJ*, **547**, L45 (2001)
17. Menou, K., Perna, R., & Hernquist, L. *ApJ*, **559**, 1032 (2001)
18. Meyer-Hofmeister, E. *A&A*, **253**, 459 (1992)
19. Nagel, T., Dreizler, S., Rauch, T., & Werner, K. *A&A*, **428**, 109 (2004)
20. van Paradijs, J., Taam, R. E., & van den Heuvel, E. P. J. *A&A*, **299**, L41 (1995)
21. Perna, R., Hernquist, L. E., & Narayan, R. *ApJ*, **541**, 344 (2000)
22. Shakura N. I., & Sunyaev R. A. *A&A*, **24**, 337 (1973)
23. Wang, Z., Chakrabarty, D., & Kaplan, D. L. *Nature*, **440**, 772 (2006)
24. Werner, K., & Husfeld, D. *A&A*, **148**, 417 (1985)
25. Werner, K. *A&A*, **161**, 177 (1986)
26. Werner, K., Deetjen, J. L., Dreizler, S., et al. in: Hubeny, I., Mihalas, D., Werner, K. (ed.) *Stellar Atmosphere Modeling*, ASP Conf. Series, **288**, 31 (2003)
27. Woods, P. M., & Thompson, C. in: Lewin, W. H. G., van der Klis, M. (ed.) *Compact Stellar X-Ray Sources*, Cambridge University Press, p. 547 (2006)